Paper No.
01040

CORROSION 2001

A Mechanistic Model for CO_2 Corrosion with Protective Iron Carbonate Films

Srdjan Nesic*, Magnus Nordsveen♣, Rolf Nyborg and Aage Stangeland§
Institute for Energy Technology
N-2027 Kjeller, Norway

ABSTRACT

The mechanistic model of uniform CO_2 corrosion is presented which covers: electrochemical reactions at the steel surface, diffusion of species between the metal surface and the bulk including diffusion through porous surface films, migration due to establishment of potential gradients and homogenous chemical reactions including precipitation of surface films. The model can predict the corrosion rate, as well as the concentration and flux profiles for all species involved. Comparisons with laboratory experiments have revealed the strengths of the model such as its ability to assist in understanding of the complex processes taking place during corrosion in the presence of surface films.

Keywords: carbon dioxide, carbon steel, CO_2 corrosion, prediction, model

INTRODUCTION

Numerous prediction models for CO_2 corrosion of carbon steel exist.[1-19] A thorough review of the field of CO_2 corrosion modelling has been published[20] in 1997. A joint industry project where several of the models were compared with actual field data has recently been finished[21]. Some of the more recent models have been based on mechanistic descriptions of the processes underlying CO_2 corrosion[14-19]. The present study describes a mechanistic model in which some of the shortcomings noted in the previously published works were corrected. Generally, the strength of the model presented below is that it describes mechanistically most of the important processes present in uniform CO_2

* Current address: Department of Mechanical Engineering, University of Queensland, Brisbane, Qld 4072, Australia.
♣ Current address: Studsvik Scandpower AS, P.O.Box 15, 2027 Kjeller, Norway.
§ Current address: Norwegian Metrology and Accreditation Service, Fetveien 99, 2007 Kjeller, Norway.

corrosion: electrochemical reactions, chemical reactions, transport of species between the metal and the bulk, transport of species through porous corrosion films, etc. Therefore, the model can with small modifications be adapted to cover other types of uniform and even localised corrosion. For example the model is currently being extended to cover uniform corrosion of mild steel in CO_2/H_2S solutions as well as flow-accelerated corrosion of carbon steel in neutral and alkaline solutions.

THE PHYSICO-CHEMICAL MODEL OF CO_2 CORROSION OF MILD STEEL

In uniform CO_2 corrosion of mild steel a number of chemical, electrochemical and transport processes occur simultaneously.

Chemical reactions

When dissolved in water, the CO_2 is hydrated to give carbonic acid:

$$CO_2 + H_2O \Leftrightarrow H_2CO_3 \tag{1}$$

which then dissociates in two steps:

$$H_2CO_3 \Leftrightarrow H^+ + HCO_3^- \tag{2}$$

$$HCO_3^- \Leftrightarrow H^+ + CO_3^{2-} \tag{3}$$

In practical CO_2 corrosion situations many other species are present in the water solution. Therefore a large number of additional chemical reactions can occur. The full list of the chemical reactions accounted for in the present version of the model is shown in Table 1.

Chemical reactions are sometimes very fast compared to all other processes occurring simultaneously, thus preserving chemical equilibrium throughout the solution. In other cases, when chemical reactions proceed slowly, other faster processes (such as electrochemical or diffusion) can lead to local non-equilibrium in the solution. Either way the occurrence of chemical reactions can significantly alter the rate of electrochemical processes at the surface and the rate of corrosion. This is particularly true when, due to high local concentrations of species solubility limit is exceeded and precipitation of surface films occurs. In a precipitation process, heterogeneous nucleation occurs first on the surface of the metal or within the pores of an existing film since homogenous nucleation in the bulk requires a much higher concentration of species. Nucleation is followed by crystalline film growth. Under certain conditions surface films can become very protective and reduce the rate of corrosion by forming a transport barrier for the species involved in the corrosion reaction and by covering (blocking) parts of the metal surface i.e. by making it "unavailable" for corrosion.

In CO_2 corrosion when the concentrations of Fe^{2+} and CO_3^{2-} ions exceed the solubility limit, they combine to form solid iron carbonate films according to:

$$Fe^{2+} + CO_3^{2-} \Rightarrow FeCO_3(s) \tag{4}$$

A number of recent publications discuss the role of iron carbonate films in CO_2 corrosion[22-24].

Electrochemical reactions at the steel surface

The presence of CO_2 increases the rate of corrosion of mild steel in aqueous solutions primarily by increasing the rate of the hydrogen evolution reaction. In strong acids, which are fully dissociated, the rate of hydrogen evolution occurs according to:

$$2H^+ + 2e^- \rightarrow H_2 \tag{5}$$

and cannot exceed the rate at which H^+ ions are transported to the surface from the bulk solution (mass transfer limit). In CO_2 solutions where typically pH >4 this limiting flux is small and therefore it is the presence of H_2CO_3 which enables hydrogen evolution at a much higher rate. Thus for pH>4 the presence of CO_2 leads to a much higher corrosion rate than would be found in a solution of a strong acid at the same pH.

The presence of carbonic acid can increase the corrosion rate in two different ways. Dissociation of H_2CO_3 serves as an additional source of H^+ ions[4], which are subsequently reduced according to equation (5). In addition there is a possibility that direct reduction of carbonic acid can increase the corrosion rate further:

$$2H_2CO_3 + 2e^- \rightarrow H_2 + 2HCO_3^- \tag{6}$$

as assumed by many workers in the field[1, 25, 26]. Both reaction mechanisms for hydrogen evolution have been included in the present model. The direct reduction of carbonic acid can be "switched on or off" in the model in order to study the effect of this additional cathodic reaction.

It has been suggested[27] that in CO_2 solutions at pH>5 the direct reduction of the bicarbonate ion becomes important:

$$2HCO_3^- + 2e^- \rightarrow H_2 + 2CO_3^{2-} \tag{7}$$

what may be the true as the concentration of HCO_3^- increases with pH and can exceed that of H_2CO_3. However it is difficult to experimentally distinguish the effect of this particular reaction mechanism for hydrogen evolution from the previous two: (5) and (6) and therefore this reaction has not been included in the model.

Hydrogen evolution by direct reduction of water:

$$2H_2O + 2e^- \rightarrow H_2 + 2OH^- \tag{8}$$

can become important[28, 29] only at p_{CO_2} <<1 bar and pH>5 and is therefore rarely an important factor in practical CO_2 corrosion situations. This reaction was also omitted from the present model.

The electrochemical dissolution of iron in a water solution:

$$Fe \rightarrow Fe^{2+} + 2e^- \tag{9}$$

is the dominant anodic reaction in CO_2 corrosion. It has been studied extensively in the past with several multi-step mechanisms suggested to explain the various experimental results. Even if the overall anodic reaction (9) does not suggest any dependency on pH, numerous studies have revealed that in strong acidic solutions the reaction order with respect to OH^- is between 1 and 2. Measured Tafel slopes are typically 30-40 mV. This subject, which is controversial with respect to the mechanism, is reviewed in detail by Drazic[30] and Lorenz and Heusler[31]. The anodic dissolution in aqueous CO_2 solutions has, until recently, not been the subject of detailed mechanistic studies. The mechanism suggested by Bockris et al.[32] for strong acids has frequently been assumed to apply in CO_2 solutions in which typically pH>4 [1, 25, 27, 33]. It was overlooked that the experimental results presented by Bockris et al.[32] show that the pH dependency decreases rapidly above pH 4 suggesting a change in mechanism or a different rate determining step. In the present study the results from a recent study by Nesic et al.[34] were used where it was confirmed that the anodic dissolution of iron does not depend significantly on OH^- concentration above pH 4 but is affected by the presence of CO_2, as previously indicated by Davies and Burstein[35] and Videm[36].

Transport processes

From the description of the electrochemical processes it is clear that certain species in the solution will be produced in the solution at the metal surface (e.g. Fe^{2+}) while others will tend to be depleted (e.g. H^+). The established concentration gradients will lead to molecular diffusion of the species towards and away from the surface. In cases when the diffusion processes are much faster than the electrochemical processes, the concentration change at the metal surface will be small. Vice versa, when the diffusion is unable to "keep up" with the electrochemical reactions, the concentration of species at the metal surface can become very different from the ones in the bulk solution. On the other hand, the rate of the electrochemical processes depends on the species concentrations at the surface. Therefore there exists a two-way coupling between the electrochemical processes at the metal surface (corrosion) and processes in the adjacent solution (i.e. diffusion). The same is true for chemical reactions which interact with both the transport and electrochemical processes in a complex way as described below.

In most practical systems the water solution is flowing. Therefore the effect of convection on transport processes cannot be ignored. Near solid surfaces, in the boundary layer, mean convection is parallel to the surface and does not contribute much to the transport of species. However, turbulent eddies can penetrate deep into the boundary layer and significantly alter the rate of species transport to and from the surface. Very close to the surface no turbulence can survive and the species are transported solely by diffusion and electromigration as described in the following paragraph.

Many of the dissolved species in CO_2 solutions are electrically charged (ions) and have different diffusion coefficients. This means that they diffuse through the solution with different "speeds". Consequently any diffusion occurring due to the existence of concentration gradients will tend to separate the charges[37]. This will be opposed by strong short-range attraction forces between opposing charges. Therefore only a small separation of charge can occur, building up to a potential gradient within the solution which will tend to "speed up" the slower diffusing ions and "slow down" the faster ones, a process called electromigration or simply migration.

THE MATHEMATICAL MODEL

A mathematical model is described below which covers all of the above processes including:

- Homogenous chemical reactions including precipitation of surface films.
- Electrochemical reactions at the steel surface;
- Transport of species to and from the bulk, including convection and diffusion through the boundary layer and the porous surface films as well as migration due to establishment of potential gradients;

These processes are mathematically modelled using fundamental equations. Parameters for the different equations, such as equilibrium constants, reaction rate constants and diffusion coefficients, are taken from the open literature.

Chemical reactions

Chemical reactions can be seen as local sources or sinks of species in the solution (term R_i in the transport equation (20) below). To describe the way the rates of chemical reactions are calculated, the first and second dissociation steps of carbonic acid will be used as an example:

$$H_2CO_3 \underset{k_{b,ca}}{\overset{k_{f,ca}}{\Leftrightarrow}} H^+ + HCO_3^- \tag{10}$$

$$HCO_3^- \underset{k_{b,bi}}{\overset{k_{f,bi}}{\Leftrightarrow}} H^+ + CO_3^{2-} \tag{11}$$

The net rate of change of carbonic acid concentration can be found from reaction (10) to be:

$$R_{H_2CO_3} = k_{f,ca} c_{H_2CO_3} - k_{b,ca} c_{H^+} c_{HCO_3^-} \tag{12}$$

where $k_{f,ca}$ and $k_{b,ca}$ are the forward and backward reaction rate constant, $c_{H_2CO_3}$, c_{H^+} and $c_{HCO_3^-}$ are the concentrations of species involved. The net rates of change R_i of the concentrations of the other three species: H^+, HCO_3^-, and CO_3^{2-} involved in these two chemical reactions can be found in a similar way. The chemical reaction terms can be conveniently grouped by using a matrix form as:

$$\begin{bmatrix} R_{H_2CO_3} \\ R_{H^+} \\ R_{HCO_3^-} \\ R_{CO_3^{2-}} \\ \end{bmatrix} = \begin{bmatrix} -1 & 0 \\ 1 & 1 \\ 1 & -1 \\ 0 & 1 \end{bmatrix} \begin{bmatrix} \left(k_{f,ca} c_{H_2CO_3} - k_{b,ca} c_{H^+} c_{HCO_3^-}\right) \\ \left(k_{f,bi} c_{HCO_3^-} - k_{b,bi} c_{H^+} c_{CO_3^{2-}}\right) \end{bmatrix} \tag{13}$$

Indeed at equilibrium all the net rates R_i are equal to zero. Generally, for any set of k chemical reactions involving i species one can write compactly:

$$R_i = a_{ik} r_k \tag{14}$$

where tensor notation applies for the subscripts, a_{ik} is the stoichiometric matrix where row i represents the i-th species, column k represents the k-th chemical reaction, and r_k is the reaction rate vector. Using this technique any number of chemical reactions can be added to the model with little effort. The advantage of this chemical reaction model is that it does not prescribe a priori whether any particular reaction will be locally or globally in equilibrium, as is often done. If the chemical reaction rates k_f and/or k_b for a particular reaction are very large, the net reaction term R_i will be much larger than the other terms in transport equations (20) giving R_i =0. This means that the concentrations of the species involved will be at equilibrium irrespective of other processes (diffusion, migration, etc.). In the case of slow reactions the concentrations of species will be determined by other terms in transport equations (20) resulting in a non-equilibrium concentration field. The equilibrium, forward and backward reaction rates values for reactions included in the present model are listed in Table 2.

A chemical reaction of particular interest is the iron carbonate precipitation/dissolution reaction. When the concentration of Fe^{2+} and CO_3^{2-} species locally exceeds the solubility limit, i.e. the ionic product $c_{Fe^{2+}} c_{CO_3^{2-}}$ is larger than the solubility limit K_{sp} conditions are met for precipitation to begin. However, for ionic products only slightly above the solubility limit and at low temperature the precipitation rate is so low that very little film is formed. Typically in order to get appreciable rates of film formation, high temperature (>60 °C) and considerable supersaturation $S = c_{Fe^{2+}} c_{CO_3^{2-}} / K_{sp}$ are required. The precipitation reaction also acts as a local sink of the ions involved.

Nucleation of crystalline films is a very difficult process to model mathematically. In addition in many corrosion situations the rate of precipitation is believed to be controlled by the crystal growth rate rather than nucleation rate. Many theories describing the mechanism and kinetics of crystalline film growth lead to a quadratic dependence on supersaturation[38]:

$$R_{gr} = k_{gr} (S-1)^2 \tag{15}$$

where R_{gr} is the rate of growth, k_{gr} is the growth rate constant. In the case of iron carbonate precipitation two studies[39, 40] have proposed somewhat different expressions for the precipitation (crystal growth) rate, and both have been tested in the present model:

according to Johnson and Tomson[39]:
$$R_{FeCO_3} = A \cdot e^{54.8 - \frac{123.0\,kJ/mol}{RT}} \cdot K_{sp} \cdot (S^{1/2} - 1)^2 \tag{16}$$

according to van Hunnik et. al.[40]:
$$R_{FeCO_3} = A \cdot e^{52.4 - \frac{119.8\,kJ/mol}{RT}} \cdot K_{sp} \cdot (S-1)(1-S^{-1}) \tag{17}$$

In these two expressions A is the surface area available for precipitation per unit volume, K_{sp} is the precipitation rate constant. According to the present model iron carbonate precipitation can occur on the steel surface or within the pores of a given porous surface film. In the porous film A is equal to the surface area of the pores per unit volume. For iron carbonate films it is hard to find values for A in the literature. Instead a value was used based on a simple calculation for a model film consisting of

spherical particles with radius of 1 - 10 μm placed in a lattice with a distance of 1 - 10 μm from particle to particle, giving $A \approx 10^5$ m^{-1}. The solubility product K_{sp} for iron carbonate is modelled as a function of temperature (°C) and ionic strength based on the IUPAC data[41] and in-house calculations done with the Thermo-Calc program[42].

Repeated observations were made that crystals usually dissolve much faster than they grow: a factor of 5 is not uncommon[38]. In most cases it can be assumed that the rate of dissolution is controlled by the rate of mass transfer of the solvated species from the surface of the crystal into the bulk solution[38].

Electrochemical reactions at the steel surface

In the first approximation, the rates of the electrochemical reactions at the metal surface depend on the electrical potential of the surface, the surface concentrations of species involved in those reactions and temperature. Since electrochemical reactions involve exchange of electrons, the reaction rate can be conveniently expressed as a rate at which the electrons are "consumed or released" i.e. in terms of an electrical current density i. Fundamental rate equations of electrochemistry relate i to the potential at the metal surface E, via an exponential relationship:

$$i = \pm i_o \cdot 10^{\pm \frac{E - E_{rev}}{b}} \tag{18}$$

which can be written down for all electrochemical reactions involved in a corrosion process such as (5, 6, and 9). The + sign applies for anodic reactions such as (9) while the – sign applies for cathodic reactions such as (5-8). Here i_o is the exchange current density, E_{rev} is a reversible potential, while b is a Tafel slope, all characteristic for a particular electrochemical reaction. In most cases i_o and E_{rev} are non-linear functions of the concentration of species involved in a particular reaction, while all three parameters are functions of temperature. Details about how these parameters are calculated are shown in Table 3.

For a corrosion process the unknown electrical potential at the metal surface E can be found from the charge balance equation at the metal surface:

$$\sum_{1}^{n_a} i_a = \sum_{1}^{n_c} i_c \tag{19}$$

where n_a and n_c are the total number of anodic and cathodic reactions respectively. In situations where external polarisation is applied (e.g. during potentiodynamic experiments, cathodic protection using "impressed" current or in electrochemical reactors) the potential E is known explicitly.

Transport processes

Species conservation equations are used to describe the transport of all the species in the solution, irrespective of whether they are involved in the electrochemical reactions at the metal surface or in the homogenous chemical reactions. A full list of species accounted for in the present version of the model is shown in Table 4. Since this is a model of uniform corrosion, a one-dimensional computational domain is sufficient, stretching from the steel surface through the pores of a surface film and the mass transfer boundary layer, ending in the bulk of the solution, as sketched in Figure 1. The

flow field is assumed to be turbulent in the bulk solution so that the transport of species on that side of the boundary layer is dominated by turbulent mixing, while in the sublayer closer to the surface and in the pores of the surface film it is controlled by molecular transport (diffusion).

The expression for transport of species i in the presence of chemical reactions which is valid both for the liquid boundary layer[37] and the porous film[43], can be described using the species conservation equation:

$$\underbrace{\frac{\partial \varepsilon c_i}{\partial t}}_{\text{accumulation}} = \underbrace{-\frac{\partial(\kappa N_i)}{\partial x}}_{\text{net flux}} + \underbrace{\varepsilon R_i}_{\substack{\text{source or sink} \\ \text{due to chemical reactions}}} \tag{20}$$

where c_i is the concentration of species i, ε and κ are the volumetric porosity and the surface permeability of the film respectively (both equal to one in the boundary layer), N_i is the flux of species i, R_i is the source or sink of species i due to all the chemical reactions in which the particular species is involved, t is time and x is the spatial coordinate.

The flux of species N_i in equation (20) has three components: diffusion, convection and migration. Turbulent convection can be described via a turbulent diffusivity concept[44], thus the flux is:

$$\underbrace{N_i}_{\text{flux}} = \underbrace{-(D_i + D_t)\frac{\partial c_i}{\partial x}}_{\substack{\text{effective diffusion} \\ \text{(diffusion + convection)}}} \underbrace{- z_i u_i F c_i \frac{\partial \Phi}{\partial x}}_{\text{migration}} \tag{21}$$

where D_i is the molecular diffusion coefficient of species i, D_t is the turbulent diffusion coefficient, z_i is the electrical charge of species i, u_i is the mobility of species i, F is the Faradays constant and Φ is the electric potential.

Not all terms in the equations (20) and (21) above are easily found. The molecular diffusion coefficients D_i for various species are readily listed in the open literature (see Table 4). The mobility u_i can best be determined via its relationship with the diffusion coefficient (Nernst-Einstein equation)[37]:

$$D_i = RTu_i \tag{22}$$

It is assumed that there is no fluid flow within the porous film (for $x<\delta_f$). The turbulent diffusivity which is used to represent the effect of turbulent convection on transport of species in the liquid boundary layer (21) is a function of the distance from the surface metal or film surface and is then given by[44]:

$$D_t = \begin{cases} 0 & \text{for } x < \delta_f \\ 0.18\left(\dfrac{x-\delta_f}{\delta-\delta_f}\right)^3 \dfrac{\mu}{\rho} & \text{for } x > \delta_f \end{cases} \tag{23}$$

The liquid boundary layer thickness is typically a function of the Reynolds number. For pipe flow it reads[44]:

$$\delta - \delta_f = 25 Re^{-7/8} d \tag{24}$$

where d is the hydraulic diameter, $Re = \rho U d/\mu$ is the Reynolds number, U is bulk velocity , ρ is the density, and μ is dynamic viscosity. The density and viscosity were modelled as a function of temperature as shown in Table 5.

In the first approximation the permeability κ of surface films for transport of species in equation (20) depends on the amount of pores in the film (expressed as superficial porosity ε_s in a plane parallel to the metal surface) and the shape and connections between the pores (expressed via the tortuosity ψ):

$$\kappa = \psi \varepsilon_s \tag{25}$$

If one assumes that superficial porosity ε_s is approximately equal to volumetric porosity ε and that tortuosity is proportional to a square root of porosity (in an analogy with the theory of porous electrodes [37]) permeability of surface films for transport of species κ can be found as

$$\kappa = \varepsilon^{3/2} \tag{26}$$

The electric potential Φ in equation (21) can be found via[37]:

$$\frac{\partial}{\partial x}\left(\kappa \xi \frac{\partial \Phi}{\partial x}\right) = -\varepsilon F \sum_i z_i c_i \tag{27}$$

where ξ is the dielectric constant and depends on temperature as indicated in Table 5. It is clear from equation (27) that the potential field $\partial\Phi/\partial x$ in the solution is established due to the charge imbalance $\sum_i z_i c_i$. In the present model a local charge imbalance will be established due to species concentration gradients and different diffusion coefficients of charged species in solution. The proportionality constant $\varepsilon F/\kappa\xi$ in equation (27) is so large that even a tiny separation of charge results in an appreciable potential gradient which in practice prevents any significant separation of charge. Often instead of equation (27) a simple electroneutrality equation is used[37]:

$$\sum_i z_i c_i = 0 \tag{28}$$

This electroneutrality equation is based on an assumption that any, however small, amount of solution is always electroneutral i.e. there is a perfect balance between the positively and negatively charged species everywhere in the solution. In other words: no charge separation can occur.

For the species transport equations (20) and the electrical potential equation (27) initial and boundary conditions must be specified. Initial conditions are given in Table 6 and boundary conditions are given in Table 7.

Growth of iron carbonate films

In the model described above the means to calculate the thickness of iron carbonate film δ_f and its porosity ε are not given. While the rate of iron carbonate precipitation can be readily calculated from expressions (16) or (17), it is not straightforward to compute the morphology of the resulting solid film precipitate.

The model can be used to predict the equivalent of a scaling tendency proposed by van Hunnik et al[40] which is a ratio between the precipitation rate and the corrosion rate before any film is formed. Two main cases can be distinguished:

- when the precipitation rate is much smaller than the corrosion rate (expressed in the same units) the result is a porous and unprotective film,
- when the precipitation rate is much higher than the corrosion rate it is very likely that dense protective iron carbonate films will form.

In the present version of the model the user can specify the thickness and porosity of up to four different layers of the corrosion product film, and simulate the corrosion processes occurring beneath the film and the transport processes through the film. In addition, the film thickness and porosity under different conditions have been correlated with a large number of corrosion loop experiments where protective corrosion films have been formed as described later in the paper.

THE NUMERICAL MODEL

All the relevant equations have been listed above. For n species in the solution one has $n+1$ equations, that is: one transport equation (20) for each species and equation (27) for the potential. Since all the equations are strongly and nonlinearly coupled through the chemical reaction and migration terms, they all have to be solved simultaneously, together with the boundary conditions including the surface charge balance equation (19).

The differential transport equations (20) were discretized using a finite difference method and a non-uniform grid as sketched in Figure 2. The finite difference approximation of the transport equations (20) the for species i in control volume j is given by:

$$\varepsilon_j \frac{c_{i,j}^{n+1} - c_{i,j}^{n}}{\Delta t} \Delta x_j = -\kappa_j N_{i,j+1/2}^{n+1} + \kappa_j N_{i,j-1/2}^{n+1} + \varepsilon_j R_{i,j}^{n+1} \Delta x_j \tag{29}$$

Superscripts $n+1$ and n denote new and old points in time, respectively, Δx_j is the size of the control volume j. A fully implicit time discretization scheme is used here for stability reasons where all the variables on the right hand side of equation (29) are taken at the new time $n+1$. Following spatial discretization, all the terms are evaluated in the center of the control volumes except the fluxes which are evaluated at the control volume boundaries (see Figure 2). Harmonic averaging is used to calculate these fluxes based on values of the variables in the node points $j-1$, j and $j+1$ on each side of the boundaries. When there is an abrupt change in permeability e.g. at the interface between the fluid and the film, other interpolation schemes would not be conservative and would lead to large numerical errors. All the nonlinear terms: the fluxes, the chemical reaction rate terms and all the terms in the surface charge balance equation are linearized in variable space. This is achieved by using Taylor series expansion around the known (old) solution and by keeping only the constant and the linear term. For example in the case of the chemical reaction terms this reads:

$$R_{i,j}^{n+1} = a_{ik} r_k^{n+1} = a_{ik} \left(r_k^n + \frac{\partial r_k^n}{\partial c_i} \left(c_{i,j}^{n+1} - c_{i,j}^{n} \right) \right) \tag{30}$$

The discretization procedure described above converts the set of nonlinear partial differential equations for species transport (20) and the electric potential (27) into a set of linear equations in the form $Ax = b$. The matrix A is block tri-diagonal. In the present study, the equations are solved directly by a LU solver[45].

The model was implemented in Fortran programming language to increase the speed of the lengthy calculations. The user interface was programmed in Microsoft Excel/Visual Basic in order to exploit the user-friendly features of this package including input/output dialogs and plotting capabilities.

COMPARISON WITH EXPERIMENTS

Any model cannot be trusted before its performance is compared with experimental values. A number of such comparisons with laboratory data are presented below.

Experiments without protective films

In order to simulate a standard laboratory corrosion experiment: a potentiodynamic sweep, the original model was slightly adapted so that the simulation was executed much in the same way as an experimental potentiodynamic sweep is done: a steady state corrosion potential/current was calculated first and then the potential was swept anodically and cathodically. This was achieved by excluding the surface charge balance equation (19) from the calculations. Instead the surface potential was specified explicitly and changed at a slow rate so that equilibrium concentrations were reached at each point. In the actual experiments, which were conducted under strictly controlled chemical, electrochemical and hydrodynamic conditions, two different flow geometries were studied simultaneously in the same electrolyte within a glass loop: a rotating cylinder and pipe flow[46]. As indicated in Figure 3 the agreement between the model predictions and the experiments is very good. It should be noted how the cathodic branch of the curve exhibits a limiting current which is a direct consequence of the slow hydration rate of CO_2 (see Table 2). Almost identical limiting currents were obtained irrespective of whether the direct reduction of carbonic acid (6) was included in the model or not. Small discrepancies exist between the predictions and the experimental values at the very low and very high overpotentials. On the cathodic side this is due to an additional electrochemical reaction (water reduction) which occurs at the very negative potentials and is not presently included in the model. On the anodic side the apparently higher Tafel slope of the measured curves probably results from prepassivation, a phenomenon also not included in the model at this stage.

The present model was then used to simulate a large number of selected flow loop corrosion experiments performed under conditions giving no or little protective film formation[47]. The experiments were performed at 20-90 °C, with the majority in the 40-60 °C range. The CO_2 partial pressure p_{CO_2} was between 0.3 and 12 bar and the flow velocity between 0.1 and 13 m/s. Low pH values in the range 3.5-4.5 were used, except for a few experiments at 20 °C with pH around 5.5. At these conditions very high corrosion rates are obtained. The agreement between the predictions and the experiments is only modest with the model generally underpredicting the corrosion rate, as seen in Figure 4. The reason is that in these long duration experiments conducting iron carbide films formed which increased the corrosion rate somewhat via a galvanic effect[47-48], a phenomenon not presently included in the model. In addition, a careful analysis has revealed that for the experiments conducted at low temperatures (20 °C) and low partial pressures of CO_2 the agreement is much better. This is also

due to the fact that most of the experimentally determined coefficients built into the model were obtained at low temperatures and CO_2 partial pressures, while theoretical relationships were typically used to extend their validity to the higher temperature and pressure ranges and need further refinement.

Correlation of corrosion film properties with loop experiments

As the thickness and porosity of the corrosion film cannot be predicted mechanistically by the present model, these parameters have been determined from a large number of corrosion loop experiments where protective corrosion films have formed. Loop experiments performed at 20 - 150 °C, pH 3.5 - 6 and p_{CO_2}=0.5 - 6 bar were used. Rules for default film thickness and porosity as function of pH and temperature were obtained which are used in the model if the user does not choose to explicitly specify the film thickness and porosity.

Film thickness was measured on SEM micrographs of specimens from a large number of corrosion loop experiments where corrosion films formed. In most of these experiments, lasting three to four weeks, the thickness of the corrosion film was between 20 and 100 μm, with 50 μm being a typical value. On the other hand, testing the model has revealed that the corrosion rate was highly dependent on the film porosity, while the dependence on film thickness was much smaller. The change in the corrosion rate achieved by increasing the film thickness from 20 to 100 μm for a given porosity was for most cases negligible. It was therefore decided to use a constant value of 50 μm as default film thickness for all conditions in the model and determine only the porosity of the corrosion film from the experimental results.

The model was run for the conditions in each loop experiment, while the film porosity for each case was adjusted to give the closest fit between the predicted corrosion rate and the measured corrosion rate at the end of the experiment. In Figure 5 the calculated porosity as function of temperature is shown for experiments at pH close to 5.8 and CO_2 partial pressure close to 2 bar. The calculated porosity increases sharply as the temperature is reduced below 80 °C, where less protective films are formed. The data can be represented with an exponential dependence. The porosity is shown as a function of pH for experiments around 80 °C and 2 bar CO_2 in Figure 6. The porosity decreases markedly with increasing pH as films with better protective properties are formed. The data can again be represented with an exponential dependence. The points with unit porosity represent several cases from experiments without films. Attempts to correlate porosity with CO_2 partial pressure in the same way were not successful, as there were too few data points with different CO_2 partial pressures to show a distinct correlation. However, increased CO_2 partial pressure increases the iron carbonate precipitation rate and can lead to denser films.

The default film porosity in the model was obtained by combining the two correlations described above. The default film porosity ε is then given by the following formula:

$$\varepsilon = A \cdot e^{-B \cdot T - C(pH+D)} + E \tag{31}$$

where A = 580, B = 0.045, C = 1.5, D = -2.2 and E = 0.06 and the temperature is given in °C. In addition the porosity at the film layer at the metal surface is set equal to $\varepsilon_1 = 0.1+0.9\varepsilon$. This is done to reduce the effect of surface coverage at low porosities. The default film thickness is always set to 50 μm except for the cases when the porosity is calculated to be one (low temperature and low pH). This means that there are no films present, and the film thickness is then set to zero.

Only specimens with uniform corrosion were used in the correlations described above. In several of the loop experiments mesa attack with high local corrosion was observed on specimens with protective films outside the mesa attack[22-24]. Beside predicting the corrosion rates both with and without corrosion films the model estimates a risk for mesa attack which is based on observations of mesa attack in loop experiments. The model reports high risk for mesa attack if the flow velocity is 5 m/s or higher and the temperature is between 60 and 120 °C. If the flow velocity is below 2.5 m/s low risk is reported. In between medium risk for mesa attack is reported.

Experiments with protective films

Predictions with the model were compared with results from loop experiments performed under conditions giving protective corrosion films. In Figure 7 measured and predicted corrosion rates are compared for experiments at 80 - 120 °C, 0.8 - 2 bar CO_2 , pH 5.0 - 5.8 and flow rate 0.5 - 7 m/s. Only specimens without mesa attack have been included. The corrosion rate at the end of the experiment was used which was measured using the polarization resistance method. The predicted corrosion rate was obtained by using the default rules for film porosity and thickness as described above. When compared, the predicted corrosion rates are generally higher than the measured ones, reflecting that the rules for default film thickness and porosity in the model are conservative. The scatter indicates that improved models are needed to describe formation of protective corrosion films.

PARAMETRIC TESTING

The capabilities of the present model go far beyond a mere prediction of a steady state CO_2 corrosion rate. For example the model can be used to explain the underlying processes governing the corrosion process for a given set of conditions. To illustrate this aspect of the model, simulations were made with and without any CO_2 gas dissolved in the water and t=20 °C, pipe diameter 0.1 m, flow velocity 1 m/s, pH 6. It is known from practice that in deaerated nearly-neutral conditions without any CO_2 gas dissolved in the water at low temperature, the corrosion rate of mild steel is low. The present model predicts 0.01 mm/y for this situation. When CO_2 gas is introduced with a partial pressure p_{CO_2} = 1 bar and with all other parameters unchanged, the predicted corrosion rate increases to 0.27 mm/y without taking into account the direct reduction of carbonic acid (6). When direct reduction of carbonic acid is included the predicted corrosion rate increases further to 0.97 mm/y what is close to experimentally observed values. This shows that an important effect of H_2CO_3 in the solution is to provide an additional source of H^+ through dissociation. In order to explain the increased corrosion rate in the presence of CO_2 it is not necessary to assume direct reduction of carbonic acid as an additional cathodic reaction, as originally proposed by de Waard and Milliams[1]. However, when included into the calculations, direct reduction of carbonic acid increases the corrosion rate even further.

The concentration and flux profiles for the case described above with direct reduction of carbonic acid included are shown in Figure 8 and Figure 9 respectively as function of the distance from the metal surface. At pH 6 there is little H^+ available in the bulk, and the fluxes of CO_2 and H_2CO_3 towards the surface are much larger than the flux of H^+ (all shown as negative in Figure 9 because these species move in the negative x direction). In the vicinity of the surface CO_2 is hydrated to H_2CO_3 which is then consumed at the metal surface, either by direct reduction or by dissociation to H^+ which is then reduced. The corrosion products HCO_3^- and Fe^{2+} are transported away from the metal surface (shown as positive fluxes in Figure 9).

Under these conditions, due to a high pH, in the vicinity of the metal surface supersaturation of iron carbonate is achieved which is a precondition for precipitation of surface films. However at 20 °C the precipitation rate constant is very low meaning that any protective film formation is unlikely, in agreement with numerous experiments[22,47].

At 80 °C the situation changes significantly. The corrosion rate without film is predicted to be 0.77 mm/y when direct reduction of carbonic acid is not taken into account and 3.6 mm/y when carbonic acid reduction is included. However, high levels of supersaturation are achieved which combined with higher precipitation rate constants leads to an appreciable rate of precipitation and formation of protective films. In the presence of protective films the corrosion rate is reduced for two reasons: diffusion of species toward and away from the surface is hindered, and the surface of the metal, where the corrosion reactions occur, is "blocked" by the attached film. Concentration profiles of the dissolved species in the solution shown in Figure 10 illustrate this. A two-layered film is assumed here with total film thickness of 10 μm. The inner layer next to the metal surface is quite dense (ε = 0.1) while the outer layer facing the solution is more open (ε = 0.6). The resulting concentration profiles show that most of the resistance for diffusion is in the dense layer of the film. The resulting corrosion rate is predicted to be 0.16 mm/y what is more than 20 times less than obtained for the same conditions without the film.

The simulations at 80 °C indicate that the assumption about direct reduction of carbonic acid may be necessary to explain the high corrosion rates found at this high temperature when protective films have not been formed. There are no experiments available for the exact conditions specified above in order to perform comparisons, but several loop experiments have been performed at 80 °C with pH 5.8, 1.8 bar CO_2 and 2.5 m/s flow velocity[23-24]. In these experiments corrosion rates between 8 and 11 mm/y were measured consistently at the beginning of the experiment before protective films were formed. Simulation of these experimental conditions with the model resulted in a corrosion rate of 1.2 mm/y without accounting for direct reduction of carbonic acid and 6.3 mm/y when carbonic acid reduction is included what is closer to experimentally observed values.

CONCLUSIONS

The mechanistic model created covers most of the processes important in uniform CO_2 corrosion: electrochemical reactions at the steel surface, diffusion of species to and from the bulk including diffusion through porous surface films, migration due to establishment of potential gradients and homogenous chemical reactions including precipitation of surface films. These processes are mathematically modelled using fundamental equations. The model simulates the corrosion rate and concentration and flux profiles for all involved species.

Comparisons with laboratory experiments have revealed the strengths of the model such as its ability to assist in understanding of the complex processes taking place during corrosion in the presence of surface films. However, the comparisons have also uncovered model's weaknesses primarily related the lack of reliable experimental data at higher temperatures and CO_2 partial pressures. Also the effects related to the presence of conducting iron carbide surface films need to be introduced if more accurate predictions are to be obtained at lower temperature and pH. It is recognised that the properties of protective iron carbonate corrosion product films are crucial in predicting the actual corrosion rate at higher temperatures and pH, and that mechanistic modelling of the morphology of the corrosion films is

a difficult task. Presently, the corrosion film thickness and porosity have been correlated empirically with results from corrosion loop experiments.

ACKNOWLEDGMENT

The present CO_2 corrosion model was developed in the joint industry project: Kjeller Sweet Corrosion V, with the following companies as participants: Shell, Elf, Total, Conoco, Agip, Statoil, Norsk Hydro, Saga Petroleum, Amoco and Siderca. The authors wish to thank these companies for their technical and financial support and the permission to publish this paper.

All the authors were employed at Institute for Energy Technology when the model was developed. Srdjan Nesic is currently with the University of Queensland, Brisbane, Australia. Magnus Nordsveen is currently with Studsvik Scandpower, Kjeller, Norway. Aage Stangeland is currently with the Norwegian Metrology and Accreditation Service, Kjeller, Norway.

REFERENCES

1. C. de Waard and D. E. Milliams, Corrosion, 31 (1975): p.131.
2. C. de Waard, U. Lotz, D.E. Milliams, Corrosion, 47 (1991): p. 976.
3. C. de Waard, U. Lotz, A. Dugstad, "Influence of Liquid Flow Velocity on CO_2 Corrosion: A Semi-Empirical Model", CORROSION/95, paper no. 128, (Houston Texas: NACE International, 1995).
4. M. R. Bonis, J.-L. Crolet, "Basics of the Prediction of the Risks of CO_2 Corrosion in Oil and Gas Wells", CORROSION/89, paper no. 466, (Houston Texas: NACE International, 1989).
5. J.-L. Crolet, M. R. Bonis, SPE Production Engineering, 6 (1991): p. 449.
6. Y. M. Gunaltun. "Combining research and field data for corrosion rate prediction". CORROSION/96, paper no. 27. (Houston Texas: NACE International, 1996).
7. A. M. K. Halvorsen, T. Søntvedt, "CO_2 Corrosion Model for Carbon Steel Including a Wall Shear Stress Model for Multiphase Flow and Limits for Production Rate to Avoid Mesa Attack", CORROSION/99, paper no. 42 (Houston,TX: NACE International, 1999).
8. "CO_2 Corrosion Rate Calculation Model", NORSOK standard No. M-506, Norwegian Technology Standards Institution, http://www.nts.no/norsok, June 1998.
9. A. J. McMahon, D. M. E. Paisley, "Corrosion Prediction Modelling - A Guide to the Use of Corrosion Prediction Models for Risk Assessment in Oil and Gas Production and Transportation Facilities", Report No. ESR.96.ER.066, BP International, Sunbury, 1997.
10. C. D. Adams, J. D. Garber, R. K. Singh, "Computer Modelling to Predict Corrosion Rates in Gas Condensate Wells Containing CO_2", CORROSION/96, paper no. 31, (Houston Texas: NACE International, 1996).
11. S. Srinivasan, R. D. Kane, " Prediction of Corrosivity of CO_2 H_2S Production Environments", CORROSION/96, paper no. 11, (Houston Texas: NACE International, 1996).
12. R. C. John et al, "SweetCor: An Information System for the Analysis of Corrosion of Steels by Water and Carbon Dioxide", CORROSION/98, paper no. 20, (Houston Texas: NACE International, 1998).

13. W. P. Jepson, C. Kang, M. Gopal and S. Stitzel,"Model for Sweet Corrosion in Horizontal Multiphase Slug Flow", CORROSION/97, paper no. 11, (Houston Texas: NACE International, 1997).
14. R. Zhang, M. Gopal, W. P. Jepson, "Development of a Mechanistic Model For Predicting Corrosion Rate in Multiphase Oil/Water/Gas Flows", CORROSION/97, paper no. 601, (Houston, TX: NACE International, 1997).
15. B. F. M. Pots, "Mechanistic Models for the Prediction of CO_2 Corrosion Rates under Multi-Phase Flow Conditions", CORROSION/95, paper no. 137, (Houston Texas: NACE International, 1995).
16. A. Anderko, R. Young, "Simulation of CO2/H2S Corrosion Using Thermodynamic and Electrochemical Models", CORROSION/99, paper no. 31, (Houston, TX: NACE International, 1999).
17. E. Dayalan, F. D. de Moraes, J. R. Shadley, S. A. Shirazi, E. F. Ribicki, "CO2 Corrosion Prediction in Pipe Flow Under FeCO3 Scale-Forming Conditions", CORROSION/98, paper no. 51, (Houston, TX: NACE International, 1998).
18. M. Sundaram, V. Raman, M. S. High, D. A. Tree, J. Wagner, "Deterministic Modeling of Corrosion in Downhole Environments", CORROSION/96, paper no. 30, (Houston, TX: NACE International, 1996).
19. M. S. High, J. Wagner, S. Natarajan, "Mechanistic Modelling of Mass Transfer in the Laminar Sublayer in Downhole Systems", CORROSION/2000, paper no. 62, (Houston, TX: NACE International, 2000).
20. S. Nesic, J. Postlethwaite, M. Vrhovac, J. Corrosion Reviews, 15, (1997): p.211
21. R. Nyborg, "Evaluation of CO_2 corrosion prediction models. Final report Kjeller Field Data Project." Report no. IFE/KR/F-2000/135, Institute for Energy Technology, 2000.
22. A. Dugstad, "Mechanism of Protective Film Formation During CO_2 Corrosion of Carbon Steel", CORROSION/98, paper no. 31, (Houston, TX: NACE International, 1998).
23. R. Nyborg, "Initiation and Growth of Mesa Corrosion Attack During CO_2 Corrosion of Carbon Steel ", CORROSION/98, paper no. 48, (Houston, TX: NACE International, 1998).
24. R. Nyborg, A. Dugstad, "Mesa Corrosion Attack in Carbon Steel and 0.5 % Chromium Steel", CORROSION/98, paper no. 29, (Houston, TX: NACE International, 1998).
25. L. G. S. Gray, B. G. Anderson, M. J. Danysh, P. G. Tremaine, "Mechanisms of Carbon Steel Corrosion in Brines Containing Dissolved Carbon Dioxide", CORROSION/89, paper no. 464, (Houston, TX: NACE International, 1989).
26. E. Eriksrud, T. Søntvedt, "Effect of Flow on CO_2 Corrosion Rates in Real and Synthetic Formation Waters", Advances in CO_2 Corrosion, Vol. 1. Proceedings of the CORROSION/83 Symposium on CO_2 Corrosion in the Oil and Gas Industry, Editors: R. H. Hausler, H. P. Goddard, p. 20, NACE, 1984.
27. L. G. S. Gray, B. G. Anderson, M. J. Danysh and P. R. Tremaine, "Effect of pH and Temperature on the Mechanism of Carbon Steel Corrosion by Aqueous Carbon Dioxide", CORROSION/90, paper no. 40, (Houston, TX: NACE International, 1990).
28. P. Delahay, J. Am. Chem. Soc., 74, (1952): p. 3497.
29. S. Nesic, J. Postlethwaite, S. Olsen, Corrosion, 52, (1996): p. 280.

30. D. M. Drazic, "Iron and its Electrochemistry in an Active State", Aspects of Electrochemistry, Vol 19, p.79, Plenum Press, 1989.
31. W. Lorenz and K Heusler, "Anodic Dissolution of Iron Group Metals", in Corrosion Mechanisms, ed. F. Mansfeld (Marcel Dekker, New York, 1987).
32. J. O .M. Bockris, D. Drazic and A. R. Despic, Electrochimica Acta, 4 (1961): p.325.
33. G. Schmitt, B. Rothman, Werkstoffe und Korrosion, 28, (1977): p.816.
34. S. Nesic, N. Thevenot, J.-L. Crolet, D. Drazic, "Electrochemical Properties of Iron Dissolution in the Presence of CO_2 - Basics Revisited", CORROSION/96, paper no. 3, (Houston, TX: NACE International, 1996).
35. H Davies and G. T. Burstein, Corrosion, 36 (1980) p. 385.
36. K. Videm, "Fundamental Studies aimed at Improving Models for Prediction of CO_2 Corrosion", Progress in the Understanding and Prevention of Corrosion, Proceedings from 10th European Corrosion Congress, Vol. 1, p.513 (Institute of Metals, London, 1993).
37. J. S. Newman, Electrochemical Systems, 2nd Edition, (Prentice Hall, Englewood Cliffs, New Jersey, 1991).
38. J.W. Mullin, Crystallization, 3rd edition, (Oxford, 1993).
39. M.L. Johnson and M.B. Tomson, "Ferous Carbonate Precipitation Kinetics and Its Impact on CO_2 Corrosion", CORROSION/91, paper no. 268, (Houston, TX: NACE International, 1991)..
40. E.W.J. van Hunnik, B.F.M. Pots and E.L.J.A. Hendriksen, "The Formation of Protective $FeCO_3$ Corrosion Product Layers in CO_2 Corrosion". CORROSION/96, paper no. 6, (Houston, TX: NACE International, 1996).
41. IUPAC. Chemical Data Series, No. 21. Stability Constants of Metal-Ion Complexes. Part A: Inorganic Ligands. Pergamon Press.
42. B. Sundman, "Thermo-Calc Version L, Users' Guide", Dept. of Materials Science and Engineering, Royal Institute of Technology, Stockholm, Sweden, 1997.
43. J. Bear, Dynamics of Fluids in Porous Media, (Dover Publications, New York, 1972).
44. J. T. Davies, Turbulence Phenomena, (Academic Press, 1972).
45. H. Press, Numerical recipes in FORTRAN : the art of scientific computing, 2nd edition, (Cambridge University Press, Cambridge 1992).
46. S. Nesic, G. Th. Solvi and S. Skjerve, British Corrosion Journal, 32, (1997): p.269.
47. A. Dugstad, L. Lunde and K. Videm, "Parametric Study of CO2 Corrosion of Carbon Steel", CORROSION/94, paper no. 14, (Houston, TX: NACE International, 1994).
48. J.-L. Crolet, N. Thevenot, S. Nesic, "Role of Conductive Corrosion Products on the Protectiveness of Corrosion Layers", CORROSION/96, paper no. 4, (Houston, TX: NACE International, 1996).
49. J. E. Oddo, M. B. Tomson, "Simplified Calculation of $CaCO_3$ Saturation at High Temperatures and Pressures in Brine Solutions". SPE of AIME, (1982): p. 1583.
50. Y. K. Kharaka et al., "Solmineq 88: A Computer Program for Geochemical Modelling of Water-Rock Interactions", Alberta Research Council, Menlo Park, California, 1989.
51. D. A. Palmer, R. van Eldik, Chem. Rev., 83, (1983): p. 651.

52. Comprehensive Chemical Kinetics, Vol. 6, pp 283-284 (Elsevier Publishing Company, Amsterdam, The Netherlands, 1972).
53. K. J. Vetter, Electrochemische Kinetik, p 406-429 (Springer-Verlag, Berlin, 1961).
54. R. H. Perry, D. Green, Perry's Chemical Engineers' Handbook, 50th edition (McGraw-Hill, 1984).
55. J. Kvarekvål, "A Kinetic Model for Calculating Concentration Profiles and Fluxes of CO_2 -Related Species Across the Nernst Diffusion Layer", CORROSION/97, paper no 5, (Houston, TX: NACE International, 1997).
56. D. R. Lide, "CRC Handbook of Chemistry and Physics", 75th edition, (CRC Press, 1995).

Table 1. Chemical reactions accounted for in the model and their equilibrium constants.

	Reaction	Equilibrium constant
Dissolution of carbon dioxide	$CO_2(g) \Leftrightarrow CO_2(aq)$	$K_{sol} = [CO_2] / p_{CO_2}$
Water dissociation	$H_2O \underset{k_{b,wa}}{\overset{k_{f,wa}}{\Leftrightarrow}} H^+ + OH^-$	$K_{wa} = [H^+][OH^-]$
Carbon dioxide hydration	$CO_2 + H_2O \underset{k_{b,hy}}{\overset{k_{f,hy}}{\Leftrightarrow}} H_2CO_3$	$K_{hy} = [H_2CO_3]/[CO_2]$
Carbonic acid dissociation	$H_2CO_3 \underset{k_{b,ca}}{\overset{k_{f,ca}}{\Leftrightarrow}} H^+ + HCO_3^-$	$K_{ca} = [H^+][HCO_3^-]/[H_2CO_3]$
Bicarbonate anion dissociation	$HCO_3^- \underset{k_{b,bi}}{\overset{k_{f,bi}}{\Leftrightarrow}} H^+ + CO_3^{2-}$	$K_{bi} = [H^+][CO_3^{2-}]/[HCO_3^-]$
Dissolution of hydrogen sulphide	$H_2S(g) \Leftrightarrow H_2S(aq)$	$K_{H_2S,sol} = [H_2S] / p_{H_2S}$
Hydrogen sulphide dissociation	$H_2S \underset{k_{b,H_2S}}{\overset{k_{f,H_2S}}{\Leftrightarrow}} H^+ + HS^-$	$K_{H_2S} = [H^+][HS^-]/[H_2S]$
Hydrogen sulphide anion dissociation	$HS^- \underset{k_{b,HS^-}}{\overset{k_{f,HS^-}}{\Leftrightarrow}} H^+ + S^{2-}$	$K_{H_2S} = [H^+][S^{2-}]/[HS^-]$
Acetic acid dissociation	$HAc \underset{k_{b,ac}}{\overset{k_{f,ac}}{\Leftrightarrow}} H^+ + Ac^-$	$K_{HAc} = [H^+][Ac^-]/[HAc]$
Hydrogen sulphate anion dissociation	$HSO_4^- \underset{k_{b,HSO_4^-}}{\overset{k_{f,HSO_4^-}}{\Leftrightarrow}} H^+ + SO_4^{2-}$	$K_{HSO_4^-} = [H^+][SO_4^{2-}]/[HSO_4^-]$
Iron carbonate precipitation	$Fe^{2+} + CO_3^{2-} \Rightarrow FeCO_3$	$K_{SP} = [Fe^{2+}][CO_3^{2-}]$

Table 2. Equilibrium (K), forward (k_f) and backward (k_b) reaction rate coefficients (note: $K = k_f / k_b$).

Constant	Source
$K_{sol} = \frac{14.5}{1.00258} \times 10^{-(2.27+5.65\times10^{-3}T_f - 8.06\times10^{-6}T_f^2 + 0.075I)}$ molar/bar	Oddo and Tomson [49]
$K_{H_2S,sol} = 10^{-0.71742672 - 0.012145427 \cdot T_C + 5.6659982\,x10^{-5}\cdot T_C^2 - 8\,1902716\,x10^{-8}\cdot T_C^3}$ molar/bar	IUPAC data [41]
$K_{wa} = 10^{-(29,3868 - 0.0737549 \cdot T_K + 7.47881\,x10^{-5}\times T_K^2)}$ molar^2	Kharaka et al. [50]
$k_{b,wa} = 7.85 \cdot 10^{10}$ $M^{-1}s^{-1}$	Delahay [28]
$K_{hy} = 2.58 \times 10^{-3}$	Palmer and van Eldik [51]
$k_{f,hy} = 10^{329.85 - 110.541 \cdot \log T_K - \frac{17265.4}{T_K}}$ s^{-1}	Palmer and van Eldik [51]
$K_{ca} = 387.6 \cdot 10^{-(6.41 - 1.594\,x10^{-3}T_f + 8.52\times10^{-6}T_f^2 - 3\,07\times10^{-5}p - 0.4772I^{1/2} + 0.1180I)}$ molar	Oddo and Tomson [49]
$k_{f,ca} = 10^{5.71 + 0.0526\,xT_C - 2.94\,x10^{-4}\,xT_C^2 + 7.91\,x10^{-7}\,xT_C^3}$ s^{-1}	Comprehensive Chemical Kinetics [52]
$K_{bi} = 10^{-(10.61 - 4.97\times10^{-3}T_f + 1.331\times10^{-5}T_f^2 - 2.624\times10^{-5}p - 1.166I^{1/2} + 0.3466I)}$ molar	Oddo and Tomson [49]
$k_{f,bi} = 10^9$ s^{-1}	estimated
$K_{H_2S} = 10^{-(15.345 - 0.045676\times T_K + 5.9666\times10^{-5}\times T_K^2)}$ *molar*	Kharaka et al. [50]
$k_{f,H_2S} = 10^4$ s^{-1}	estimated
$K_{HS^-} = 10^{-(23.93 - 0.030446\times T_K + 2.4831\times10^{-5}\times T_K^2)}$ *molar*	Kharaka et al. [50]
$k_{f,HS^-} = 1$ s^{-1}	estimated
$K_{HAc} = 10^{-(6.66104 - 0.0134916\times T_K + 2.37856\times10^{-5}\times T_K{}^2)}$ molar	Kharaka et al. [50]
$k_{f,HAc} = 3.2 \cdot 10^5$ s^{-1}	Vetter [53]
$K_{HSO_4^-} = 10^{1.54883 - 0.00998\,xT_K - 5.9254\,x10^{-6}\,xT_K^2}$ molar	Kharaka et al. [50]
$k_{f,HSO_4^-} = 1$ s^{-1}	estimated

Note: in the table above T_f is temperature in degrees Fahrenheit, T is absolute temperature in Kelvin, T_C is temperature in degrees Celsius, I is ionic strength in molar and p is the pressure in psi.

Table 3. Electrochemical parameters for the reactions included in the model which fit the general rate equation: $i = \pm i_o \cdot 10^{\frac{E-E_{rev}}{b}}$,

where the exchange current density is: $i_o = \left(\frac{c_{H^+}}{c_{H^+ref}}\right)^{a_1}\left(\frac{c_{CO_2}}{c_{CO_2ref}}\right)^{a_2}\left(\frac{c_{H_2CO_3}}{c_{H_2CO_3ref}}\right)^{a_3} \cdot e^{\frac{-\Delta H}{R}\left(\frac{1}{T}-\frac{1}{T_{ref}}\right)}$

	i_{oref}	a_1	c_{H^+ref}	a_2	c_{CO_2ref}	a_3	$c_{H_2CO_3ref}$	ΔH	T_{ref}	E_{rev}	b
	$\frac{A}{m^2}$		molar		molar		molar	$\frac{kJ}{mol}$	°C	V	V
$2H^+ + 2e^- \rightarrow H_2$	0.05	0.5	10^{-4}	0	N/A	0	N/A	30	25	$-\frac{2.3RT}{F}pH$	$\frac{2.3RT}{2F}$
$2H_2CO_3 + 2e^- \rightarrow H_2 + 2HCO_3^-$	0.06	-0.5	10^{-5}	0	N/A	1	10^{-4}	50	20	$-\frac{2RT}{F}pH$	$\frac{2.3RT}{2F}$
$Fe \rightarrow Fe^{2+} + 2e^-$	1	1 for p_{CO_2} <1bar 0 for p_{CO_2} 1bar	10^{-4}	2 for pH<4 1 for 4<pH<5 0 for pH>5	0.0366	0	N/A	37.5	25	-0.488	0.03 for pH<4 0.08 for 4<pH<5 0.12 for pH>5

Note: ΔH is activation energy and T_{ref} is the reference temperature. Data and mechanisms were taken from reference [29] for the cathodic reaction and the reference [34] for the anodic reaction.

Table 4. Species accounted for in the present version of the model and the corresponding reference molecular diffusion coefficient.

Species	Diffusion coefficient (m^2/s)	Source
CO_2	$1.96 \cdot 10^{-9}$	Perry[54]
H_2CO_3	$2.00 \cdot 10^{-9}$	Kvarekvål[55]
HCO_3^-	$1.105 \cdot 10^{-9}$	Newman[37]
CO_3^{2-}	$0.92 \cdot 10^{-9}$	Kvarekvål[55]
H^+	$9.312 \cdot 10^{-9}$	Newman[37]
OH^-	$5.26 \cdot 10^{-9}$	Newman[37]
Fe^{2+}	$0.72 \cdot 10^{-9}$	Kvarekvål[55]
Cl^-	$2.032 \cdot 10^{-9}$	Newman[37]
Na^+	$1.334 \cdot 10^{-9}$	Newman[37]
Ca^{2+}	$0.792 \cdot 10^{-9}$	Newman[37]
Ba^{2+}	$0.847 \cdot 10^{-9}$	Newman[37]
Sr^{2+}	$0.791 \cdot 10^{-9}$	Newman[37]
HAc	$1.24 \cdot 10^{-9}$	Perry[54]
Ac^-	$1.089 \cdot 10^{-9}$	Newman[37]
H_2S	$1.61 \cdot 10^{-9}$	Perry[54]
HS^-	$2.00 \cdot 10^{-9}$	estimated
S^{2-}	$2.00 \cdot 10^{-9}$	estimated
HSO_4^-	$1.33 \cdot 10^{-9}$	Newman[37]
SO_4^{2-}	$1.065 \cdot 10^{-9}$	Newman[37]

Table 5. Liquid properties as a function of temperature (source: CRC Handbook of Chemistry and Physics[56]).

Dynamic viscosity	$\mu = 0.001002 \cdot 10^{\frac{1.3277\cdot(293.15-T)-0.001053\cdot(298.15-T)^2}{T-168.15}}$	kg/ms
Density	$\rho = \left(753.596 + 1.87748 \cdot T - 0.003564 \cdot T^2\right)$	kg/m^3
Dielectric constant	$\xi = \frac{10^{-9}}{36\pi} \times (249.21 - 0.79069 \times T + 0.00072997 \times T^2)$	
Diffusion coefficient (subscript *ref* denotes reference values, see Table 4)	$D_i = D_{ref} \frac{T}{T_{ref}} \frac{\mu_{ref}}{\mu}$	

Table 6. Initial conditions for the transport and electrical potential equations

species transport equations (20)	species in chemical equilibrium (R_i=0)
electrical potential equation (27)	constant (reference) potential value

Table 7. Boundary conditions for the transport and electrical potential equations

	Metal surface side	Bulk solution
species transport equations (20)	given concentration gradient: calculated via equation (18) and $N_i = i/zF$ for electroactive species zero for others	given concentration: calculated from species in chemical equilibrium (R_i=0)
electrical potential equation (27)	given potential: a constant (reference) value	given potential gradient: calculated from: $\frac{d\Phi}{dx} = -\frac{F}{\chi}\sum_i z_i D_i \frac{dc_i}{dx}$

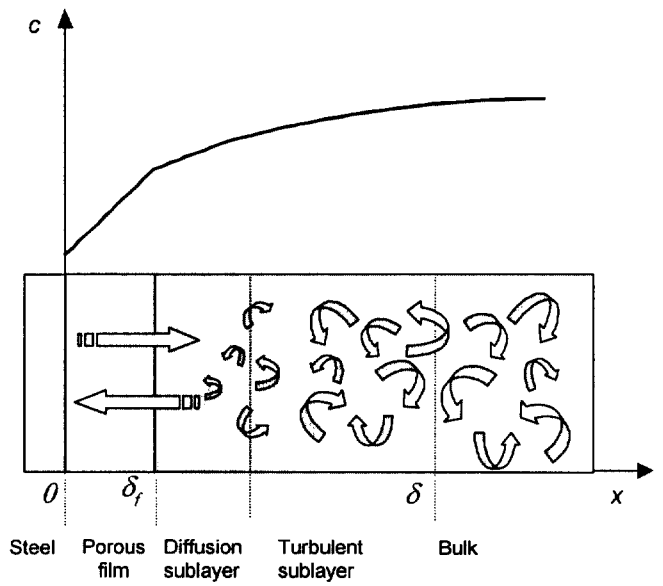

Figure 1. Sketch of the calculation domain; δ_f is the surface film thickness, δ- δ_f is the liquid boundary layer thickness. The curve on the top represents a typical variation of a single species concentration expected from theory.

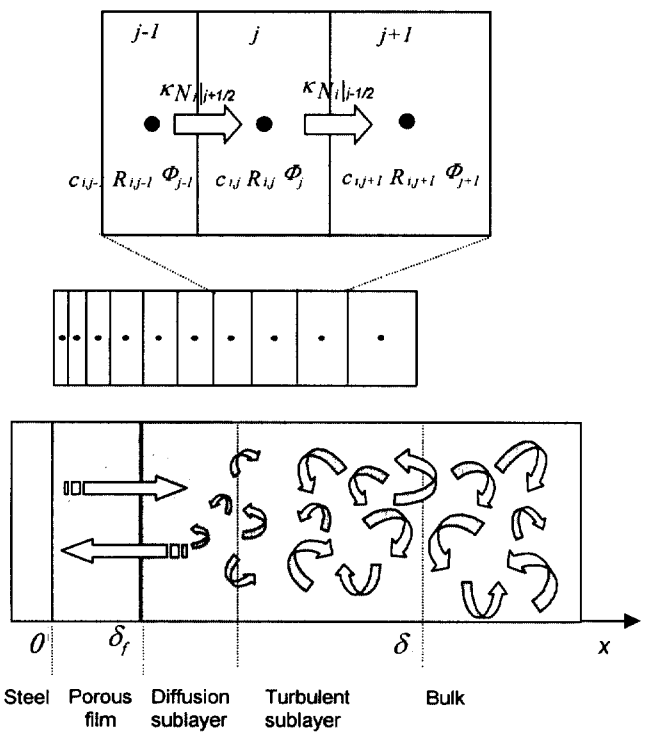

Figure 2. Sketch of the computational grid and the control volumes used for discretization of the computational domain. The concentrations, the potential and the chemical reaction terms are all computed in the centre of the control volume while the fluxes are computed on the interfaces.

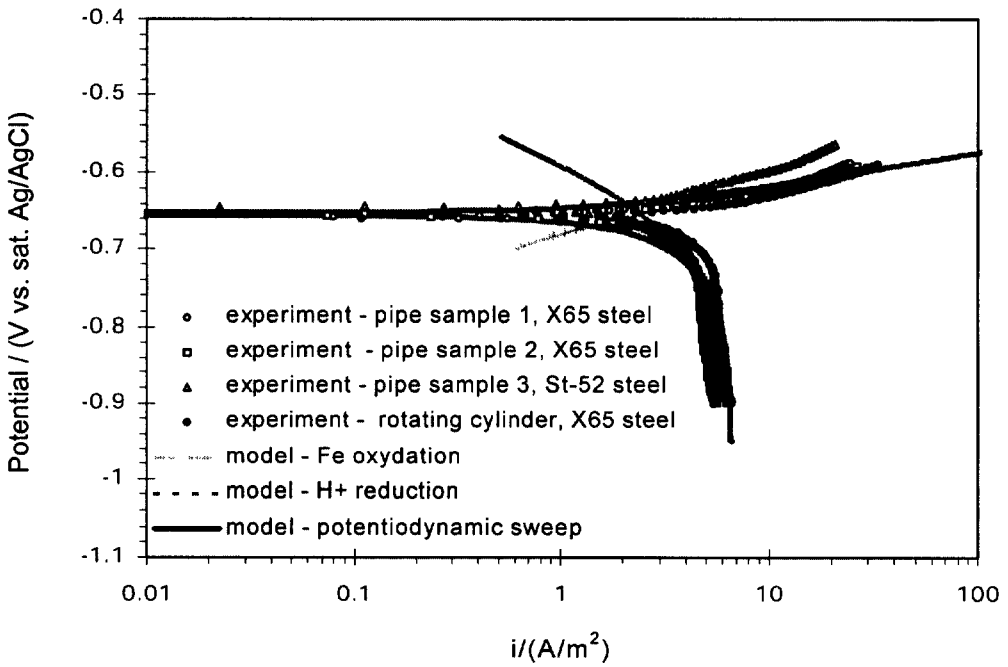

Figure 3. Comparison between predicted and measured potentiodynamic sweep for the case of CO_2 corrosion of carbon steel (experimental data taken from Nesic et al.[46]); 20°C, velocity 2 m/s, pH 4, p_{CO_2} =1 bar.

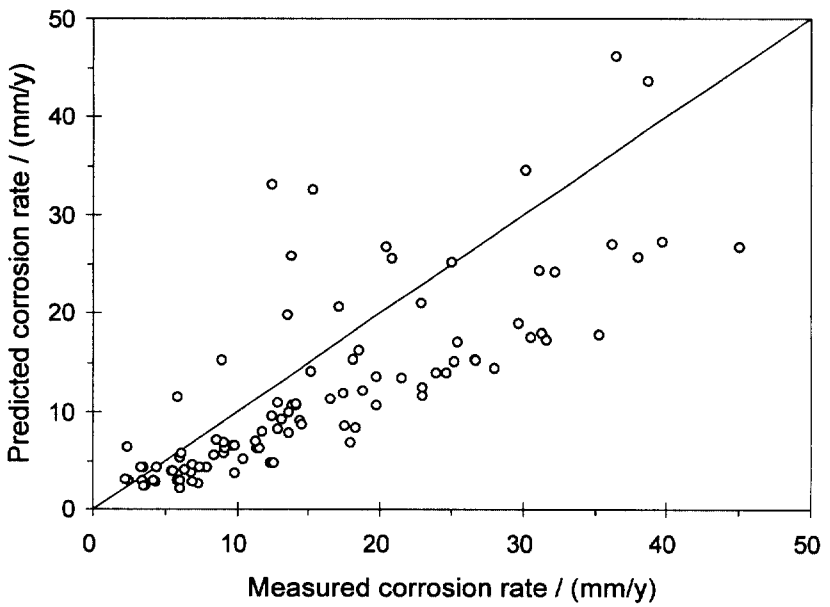

Figure 4. Comparison between predicted and measured corrosion rates in long duration flow loop corrosion experiments without protective films (experimental data taken from Dugstad et al.[47]); 20 - 90 °C, 0.1 – 13 m/s, p_{CO_2} = 0.3 - 12 bar and pH 3.5 - 6.

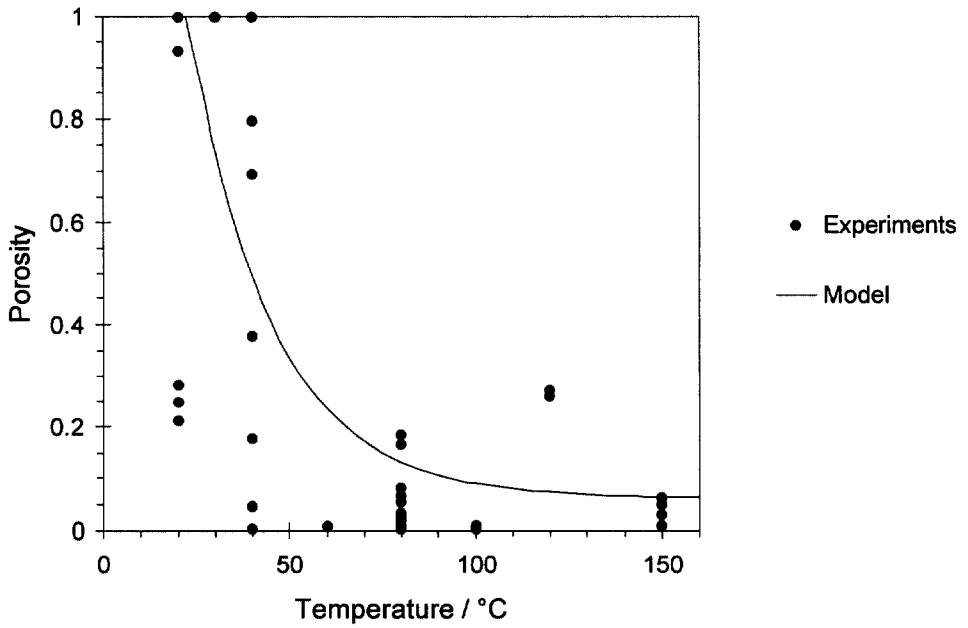

Figure 5. Porosity as a function of temperature at pH 5.8 and p_{CO_2} =2 bar. Porosity calculated from corrosion rates measured in loop experiments.

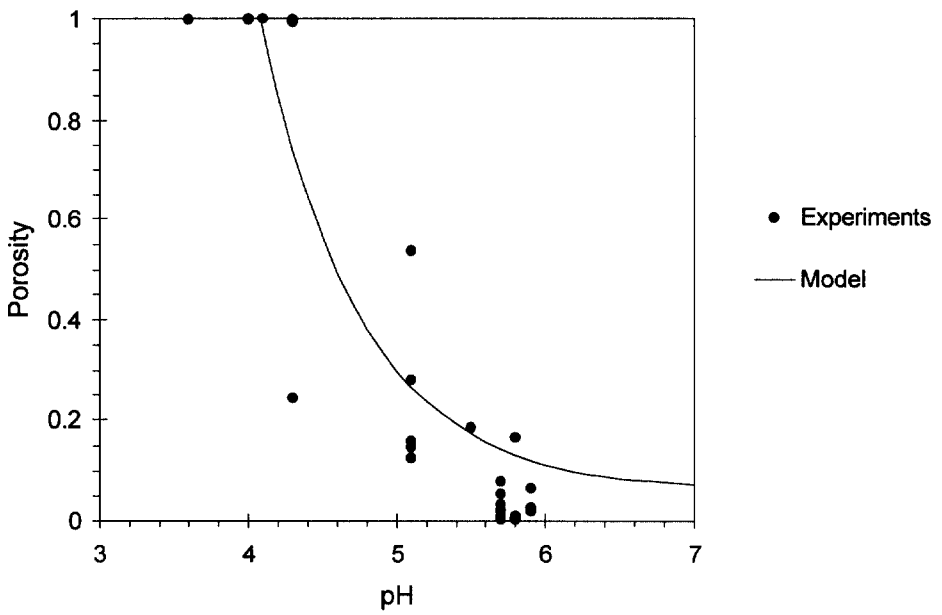

Figure 6. Porosity as function of pH at 80 °C and p_{CO_2} =2 bar. Porosity calculated from corrosion rates measured in loop experiments.

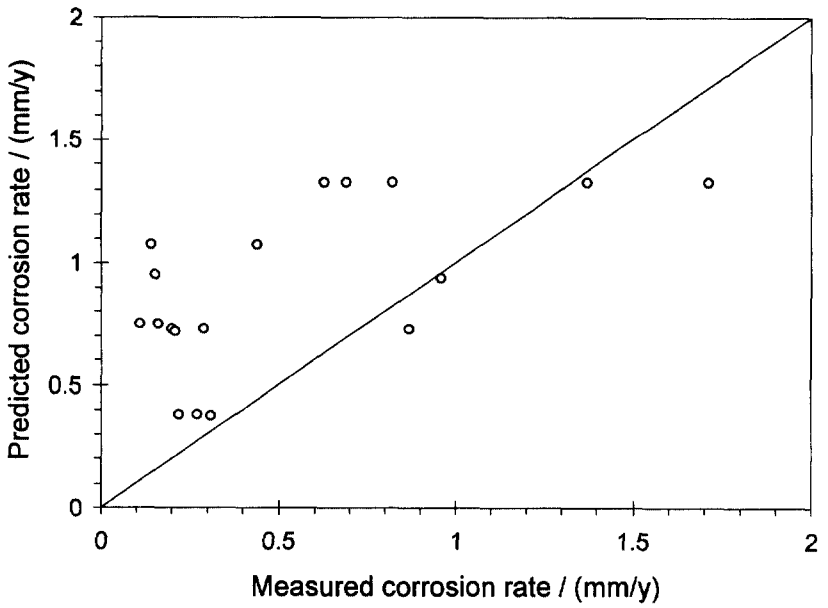

Figure 7. Comparison between measured corrosion rates in loop experiments with protective corrosion films and predicted corrosion rates with film. Experiments at 80 - 120 °C, p_{CO_2} =0.8 - 2 bar and pH 5.0 - 5.8.

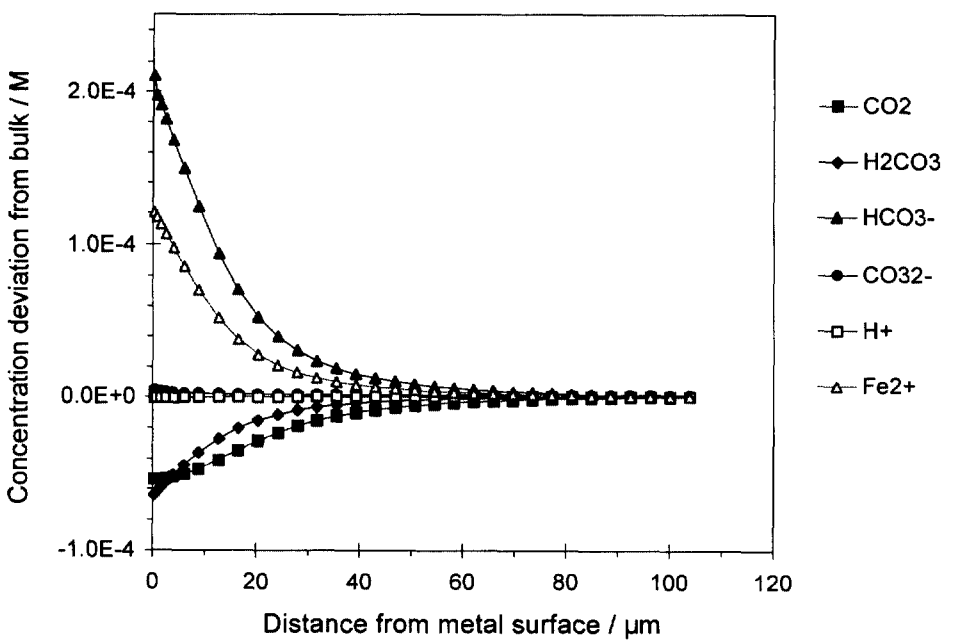

Figure 8. Deviation of dissolved species concentrations from the bulk values as a function of distance from the steel surface; 20 °C, pipe diameter 0.1 m, flow velocity 1 m/s and pH 6, p_{CO_2} = 1 bar.

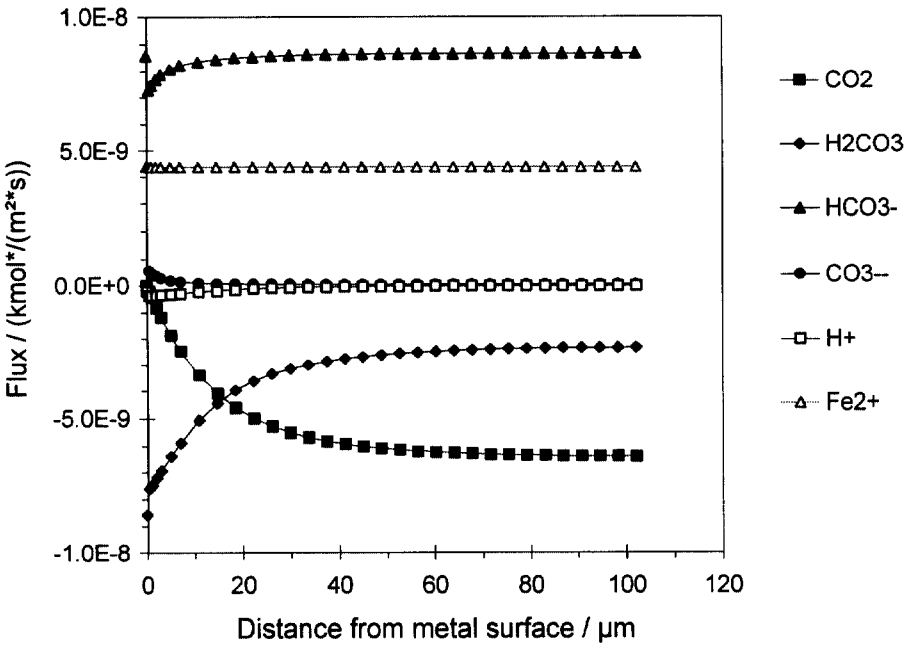

Figure 9. Flux of dissolved species as a function of distance from the steel surface; 20°C, pipe diameter 0.1 m, flow velocity 1 m/s and pH 6, p_{CO_2} = 1 bar.

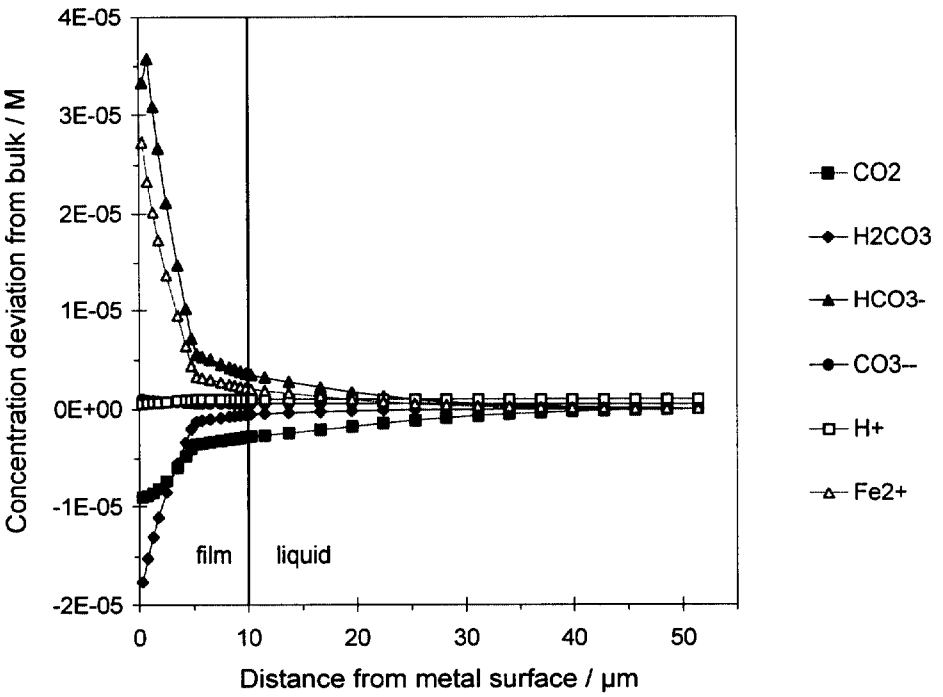

Figure 10. Deviation of dissolved species concentrations from bulk values as a function of distance from the steel surface; two-layered surface film 10 µm thick, porosity 0.1 next to the metal surface and 0.6 toward the bulk solution, 80 °C, pipe diameter 0.1 m, flow velocity 1 m/s, pH 6, p_{CO_2} =1 bar.